INSTITUTE OF PHYSICS PUBLISHING PLASMA SOURCES SCIENCE AND TECHNOLOGY
Plasma Sources Sci. Technol. **16** (2007) S115–S122 doi:10.1088/0963-0252/16/1/S13

Modelling of a low-pressure N_2–O_2 discharge and post-discharge reactor for plasma sterilization

C D Pintassilgo[1,2], K Kutasi[1] and J Loureiro[1]

[1] Centro de Física dos Plasmas, Instituto Superior Técnico, Lisboa 1049-001, Portugal
[2] Departamento de Física, Faculdade de Engenharia da Universidade do Porto, Porto 4200-465, Portugal

Received 27 July 2006, in final form 19 December 2006
Published 31 January 2007
Online at stacks.iop.org/PSST/16/S115

Abstract
A model is used to study the afterglow of a flowing microwave discharge at $\omega/(2\pi) = 2450$ MHz, $p = 667$ Pa (5 Torr), in the mixture N_2–xO_2, with $x = 0.7$–7% of O_2. This model considers a self-consistent kinetic description of the discharge and early-afterglow regions, followed by a 3D hydrodynamic analysis of the post-discharge chamber. The behaviour of NO(B) molecules and O(^{3}P) atoms is discussed in detail, since these two species play an important role in the sterilization process, respectively, due to the UV emission associated with the NO_β bands and due to erosion effects. The present work shows that a maximum in the UV emission intensity from NO_β occurs in the range 0.7–2% of O_2 added to the mixture, which is in agreement with the survival curves of spores presented by Philip *et al* (2002 *IEEE Trans. Plasma Sci.* **30** 1429). In general, the oxygen atoms concentration is more important as the added O_2 percentage increases. The interplay of N(^{4}S), O(^{3}P), NO(X), $N_2(X, v)$ and NO(B) species in the overall kinetics both in the discharge and in the early-afterglow region is discussed. Particular attention is devoted to the density of NO(B) and O(^{3}P) in the sterilization vessel at different spatial planes and for various mixture compositions.

1. Introduction

In the last few years, gas plasma sterilization in hospitals has appeared as a very promising alternative to conventional sterilization processes [1]. Investigations in [2, 3] have shown that an almost total inactivation of an initial spore population of 10^6 can be achieved using the afterglow of a reduced pressure (267–933 Pa) microwave N_2–O_2 discharge, with a small O_2 addition of the order of 0.2–2%, as a result of UV photons emitted by NO(B) state molecules and the effect of impinging O(^{3}P) atoms. As discussed in [2, 3] and also in [4], there is a combined effect between these two species during the sterilization processes. In these works, the authors claim that the sterilization process at reduced pressures is performed in three successive phases as a function of exposure time: at the beginning—1st phase—the UV photons destroy the most exposed micro-organisms. Then, in order to keep the effect of UV radiation, there is a need for the removal of these inactivated micro-organisms. It is especially at this time—2nd phase—of the sterilization process that a synergistic effect occurs between the O(^{3}P) atoms and UV photons emitted by the NO(B) excited state in the 250–320 nm spectral range (NO_β bands). The oxygen atoms contribute to the erosion of the inactivated micro-organisms, but this etching mechanism is also enhanced by UV photons. Finally, at a 3rd phase, the last living spores are exposed to UV photons. These authors have recently shown [5] that the sterilization processes can occur in two phases, in which the second phase could inactivate spores that are shielded by others and which needed more radiation to accumulate a lethal UV dose [6].

This behaviour is described by survival curves, which plot the logarithm of the number of surviving micro-organisms as a function of exposure time to the sterilizing agent. In [2], a sample with *Bacillus subtilis* was exposed to a flowing afterglow of a microwave discharge operating at $\omega/(2\pi) = 2450$ MHz and $p = 667$ Pa (5 Torr) and fractional percentages

$[O_2]_0/N_g \leqslant 7\%$ (N_g denoting the gas number density and $[O_2]_0$ the initial oxygen introduced in the mixture). For lower $[O_2]_0/N_g$ percentages equal to 0.7%, 1.5% or 2%, sterilization was achieved in less than 40 min; however, for $[O_2]_0/N_g = 4\%$ and 7%, it took 80 min and 120 min to reach sterilization.

With the aim of understanding this behaviour and to have an insight into the kinetics of a post-discharge from a low-pressure N_2–O_2 flowing microwave discharge, we report here the results from our more recent investigations involving a complete self-consistent model to describe the three different regions that constitute the N_2–O_2 sterilizer system, of the type used in [2], which includes the microwave discharge, the early-afterglow and the sterilizing (post-discharge) chamber. The purpose of this paper is twofold: (i) whereas in our previous publications the analysis has been mostly directed towards the discharge and early-afterglow region existing immediately after the end of the discharge, in the case of [7], and to the discussion of the afterglow expansion in a large volume reactor in [8], here we integrate this discussion by bridging the influence between both zones, which was not fully achieved in the previous papers; (ii) on the other hand, this system involves a large number of active species governed by a complex interplay kinetics, so that in this paper other aspects of the kinetics are presented and discussed, also involving different species. Finally, we have also chosen different experimental conditions, namely a different pressure value and discharge tube radius.

The organization of this paper is as follows. In the next section, we present the basic aspects of the full model developed to describe the discharge, the early-afterglow and the remote-afterglow region, i.e. the sterilization chamber. In section 3 we report and discuss the results of the model. Finally, in section 4 we summarize the main points of the present work.

2. Model

The model presented in this work involves the study of the three following regions: (i) the plasma source; (ii) the discharge early afterglow; and (iii) the long-lived afterglow in the sterilization vessel of much larger dimensions, where the objects to be sterilized are placed. These three regions are consecutively described by a steady-state kinetic model, a time-dependent kinetic model and a three-dimensional hydrodynamic model.

The model, the selected rate coefficients and the pertinent references have been presented and discussed in our previous publications concerned with the discharge and early afterglow [7] and with the remote afterglow [8], so that the reader should refer to those two papers for details. The only exception in relation to those papers is the inclusion of the kinetics of the $NO_2(A)$ state in the post-discharge reactor which has been disregarded in [8]. Here, we just recall that for the discharge description, we calculate the electron energy distribution function (EEDF), the vibrational distribution functions (VDFs) of $N_2(X, v)$ and $O_2(X, v)$, as well as the concentrations of the electronic excited states $N_2(A, B, B', C, a, a', w)$, and $O_2(a, b)$, together with the most important positive and negative ions, $N_2^+(X, B)$, N_4^+, O_2^+, O^+, NO^+ and O^-, and the most important neutral and excited species produced in a N_2–O_2 mixture, namely $N(^4S, {}^2D, {}^2P)$, $O(^3P)$, O_3, $NO(X, A, B)$ and $NO_2(X, A)$.

These calculations consider a steady-state kinetic model based on the solutions to the homogeneous Boltzmann's equation coupled to a system of rate balance equations for the species indicated above, where the reduced sustaining electric field in the plasma is self-consistently calculated using the requirement that, under steady-state conditions, the total rate of ionization must compensate exactly for the rate of electron loss by diffusion to the wall plus that of electron–ion recombination. This requirement ensures that the quasi-neutrality condition is obtained.

Once the stationary concentrations of the heavy species produced in the discharge are calculated, we consider their values as initial conditions in a set of coupled time-dependent kinetic master equations, including the vibrational distribution of $N_2(X, v)$ molecules. Hence, we obtain the temporal evolution of the most important heavy species produced in the afterglow.

We are then able to know the concentrations of the species at the entrance of the larger sterilization vessel. For this region, a 3D hydrodynamic model has recently been developed [8], which considers (i) the continuity equations for the different species, (ii) a sole momentum conservation equation for all species and (iii) the energy conservation equation. The 3D model, in particular, takes into account the following species: N_2 and O_2 molecules in their ground-state, $N(^4S)$ and $O(^3P)$ atoms and the species $N_2(A)$, $O_2(a, b)$, $NO(X, A, B)$, $NO_2(X)$ and O_3, which are the most populated neutral and excited molecules existing in the post-discharge chamber. In what concerns the species considered only in the discharge and early-afterglow region, including the ions, they are not taken into account in the fluid model, since their concentrations are negligibly small at the entrance of the reactor chamber. The 3D model gives as a result the distribution of the velocity vector, the gas temperature and the concentrations of a selected number of species in the reactor.

The surface loss of atoms due to re-association on the wall is not considered in the post-discharge reactor because of its large dimensions. In the discharge and early-afterglow regions, these processes are assumed to be of first order with experimental probabilities for a Pyrex surface according to [10]. In principle, the use of an experimental value should reduce the effect of possible second-order mechanisms, such as three-body collisions on the wall.

3. Results and discussion

The results have been obtained for the same conditions as in [2], which correspond to a flowing afterglow of a microwave discharge operating at $\omega/(2\pi) = 2450$ MHz, in a Pyrex tube of inner radius $R = 3 \times 10^{-3}$ m, $p = 667$ Pa and with fractional oxygen percentages $[O_2]_0/N_g \leqslant 7\%$, where N_g is the gas number density and $[O_2]_0$ is the initial oxygen concentration added to N_2 in the mixture. The discharge and the early-afterglow region are connected directly to a reactor of dimensions $0.65 \times 0.25 \times 0.25$ m^3, where the only difference from the device presented in [2] is that we consider here, for the sake of simplicity, the gas exit to be located on the top plane instead of the bottom one. However, we note that

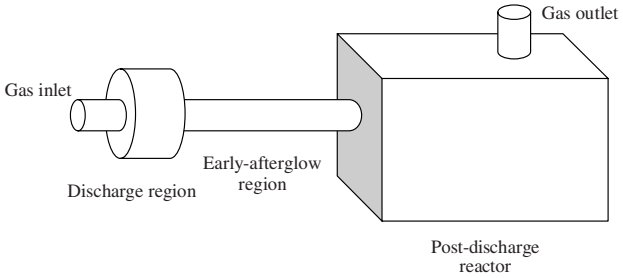

Figure 1. Schematic representation of the flowing afterglow sterilizer, which is the object of our modelling study.

there are no differences between the two situations, since the gravity force does not play any role at these densities and, also, because the inlet and outlet are symmetrically positioned on the west and top walls, respectively, so that only one half of the chamber needs to be considered in the simulation. A schematic representation of the plasma-afterglow sterilizer set-up used in the calculations is shown in figure 1.

Our calculations start with the description of the discharge region, as we first need to know the concentrations at the end of this region, that is at the beginning of the near afterglow, where we assume that the discharge electron density corresponds to the critical density for surface wave mode propagation. The surface wave mode can only propagate provided the electron density is larger than the critical value obtained from $\omega_{pe} > \omega\sqrt{1+\varepsilon_g}$, where ω_{pe} is the electron plasma angular frequency [11]. In the case of a fused silica tube ($\varepsilon_g = 4$) and $\omega/(2\pi) = 2450$ MHz, we have a critical value for the electron density equal to $3.74 \times 10^{17}\,\mathrm{m}^{-3}$.

After the early-afterglow region that exists downstream from the discharge in the same tube, our calculations continue with a 3D description of the sterilization chamber by considering the concentration of the heavy neutral species at the entrance of the reactor as being the same as those obtained in the near-afterglow region. The length of this zone is an input parameter of the model, which, associated with the gas flow rate of 500 sccm considered here, allows us to obtain the flight-time of the active species. Finally, another important input parameter in our calculations is the gas temperature. In this work, we consider 1000 K, 500 K and 300 K, respectively, in the discharge, early-afterglow region and walls of the afterglow chamber.

We present in figures 2 and 3 the predicted results for the most relevant species for sterilization purposes existing in the discharge. Figure 2 shows the fractional concentrations of the ground-state atoms $N(^4S)$ and $O(^3P)$ with respect to the total gas number density, as a function of the initial molecular oxygen added into the mixture. We observe an almost linear increase in the oxygen atom concentration with $[O_2]_0/N_g$ within the range 0–7%, whereas for the concentration of nitrogen atoms there is a slight decrease. For low concentrations of O_2, in a nitrogen–oxygen mixture at $p = 667$ Pa, the O-atoms are mainly produced by the reaction $N(^4S)+NO(X) \rightarrow N_2(X, v \sim 3)+O$, whereas the dissociation of O_2 by electron impact has only a minor role [9]. The principal loss mechanism of oxygen atoms species is the re-association on the wall. In what concerns the $N(^4S)$ atoms, we must note that the kinetics of this species in an

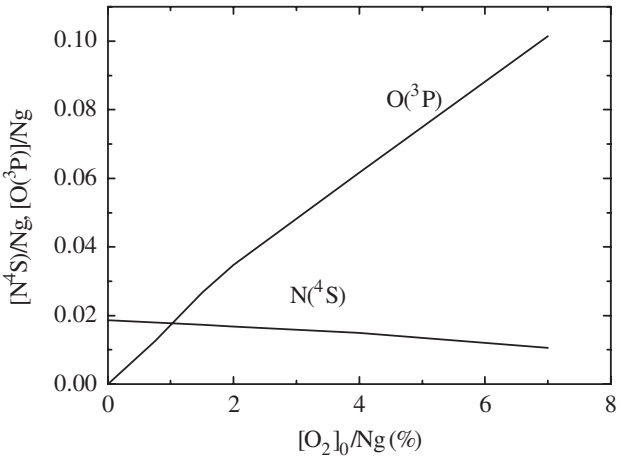

Figure 2. Fractional concentrations of $N(^4S)$ and $O(^3P)$, as a function of the initial relative O_2 concentration in a N_2–O_2 microwave discharge with $p = 667$ Pa, $\omega/(2\pi) = 2450$ MHz and $R = 3 \times 10^{-3}$ m.

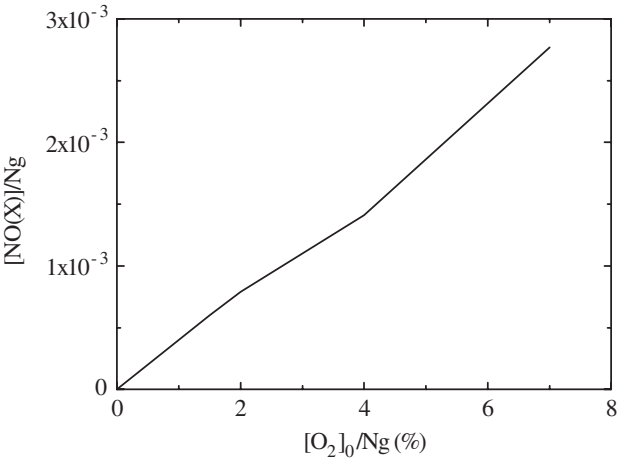

Figure 3. Fractional concentration of $NO(X)$ against the relative O_2 concentration in the discharge for the same conditions as in figure 2.

N_2–O_2 mixture is strongly correlated with $NO(X)$ through the following two processes: $N_2(X, v \geqslant 13)+O \rightarrow N(^4S)+NO(X)$ and $N(^4S)+NO(X) \rightarrow N_2(X, v \sim 3)+O$.

For completeness, figure 3 reports the fractional concentration of $NO(X)$ for the same conditions as in figure 2. Our calculations show that this species becomes more abundant as $[O_2]_0/N_g$ increases within the range of O_2 percentages investigated here. Besides the process $N_2(X, v \geqslant 13)+O \rightarrow N(^4S)+NO(X)$, another very efficient mechanism for producing $NO(X)$ at $p = 667$ Pa involves collisions between the $N_2(A)$ metastable molecules and oxygen atoms, $N_2(A)+O \rightarrow N(^2D)+NO(X)$. The production of $NO(X)$ depends then on the concentration of oxygen atoms, which, as we have shown above, increases with O_2 percentage. Furthermore, the depopulating mechanism of $NO(X)$ via the collisions with $N(^4S)$ becomes less important with the increase in $[O_2]_0/N_g$.

Since UV radiation plays a major role in the plasma sterilization process, we present in figure 4 the predicted fractional concentrations of $NO(A)$ and $NO(B)$ molecules as a function of the molecular oxygen added to N_2 in the discharge,

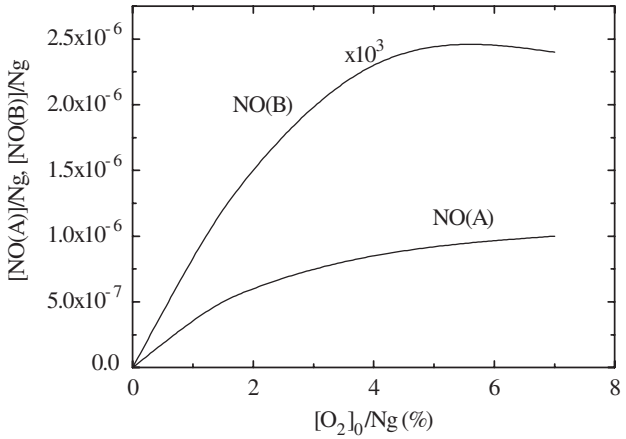

Figure 4. Fractional concentrations of the upper emitting states NO(A) and NO(B), as a function of the relative O_2 concentration in the discharge for the same conditions as in figure 2.

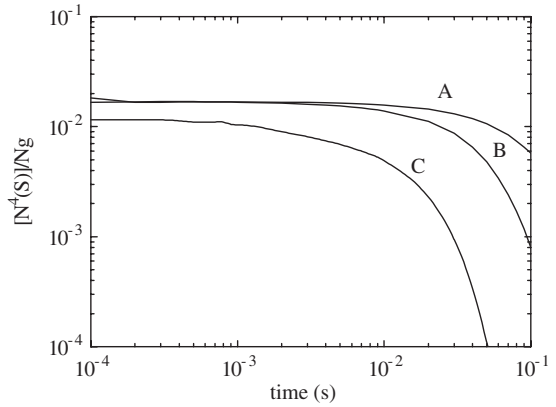

Figure 5. Temporal evolution of the fractional concentration of N(^{4}S) atoms in the afterglow of a N_2–O_2 microwave discharge with $p = 667$ Pa, $\omega/(2\pi) = 2450$ MHz, $R = 3 \times 10^{-3}$ m and the following O_2 percentages: (A) 0.7%; (B) 2%; (C) 7%.

for the same conditions as in the previous figures. We recall that these two excited states are the upper levels responsible for the UV emission of the NO_γ and NO_β bands, respectively.

Figure 4 shows that the population of the NO(A) molecules increases with the O_2 percentage. The NO(A) state is populated only by collisions of $N_2(A)$ with NO(X), $N_2(A)$+NO(X) $\rightarrow N_2(X)$+NO(A), and destroyed via radiative decay and by quenching with O_2 and NO(X). With respect to the fractional concentration of the NO(B) excited state, this figure shows that this species increases as molecular oxygen is added to the discharge. However, for $[O_2]_0/N_g \geqslant 5\%$, there is a slight decrease in the concentration of this species. The production of the NO(B) state results from the three-body mechanism N+O+(M)$\rightarrow$NO(B)+(M), with M= (N_2,O_2), while its destruction occurs by radiative decay and by quenching with N_2 and NO(X). The NO(B)+NO(X) $\rightarrow$NO(X)+NO(X) process is responsible for the predicted decrease in NO(B) for O_2 percentages larger than 5%.

The results that we have presented for the discharge could suggest that the optimizing working conditions for sterilization, in a N_2–O_2 mixture with up to 7% of added oxygen, are achieved for the highest O_2 percentages admixed into the mixture. In fact, we can see from figure 3 that the highest concentrations of oxygen atoms, which are very important for spores inactivation due to their erosion action, are obtained for $[O_2]_0/N_g = 7\%$. On the other hand, as shown in figure 4, the UV radiation from the NO_γ and NO_β bands is more important when $[O_2]_0/N_g \sim 5$–7%.

However, the survival curves presented in [2] clearly show that the shortest sterilization time occurs for $[O_2]_0/N_g \sim 0.7$–2%. Although there seems to exist a discrepancy here, we must keep in mind that the results presented so far have been obtained in the discharge. Our results for the afterglow will clear in part this point.

As referred above, the early-afterglow of the flowing discharge has been considered in the same tube as in the case of the discharge. We will present here the results predicted by the time-dependent kinetic model for a flight-time between 10^{-4} and 10^{-1} s. In this range, a very fast relaxation of the EEDF has already occurred [12]. Moreover, at afterglow times as small as 10^{-7}–10^{-6} s, the excitation rate coefficients of the $N_2(B)$ and the $N_2(A)$ states have already decreased by several orders of magnitude. Hence, we may assume in our calculations that the role played by electron impact processes in the time-dependent system of master rate balance equations is negligibly small.

Owing to the purposes of this work, we will keep focusing our analysis on the most pertinent heavy species produced in N_2–O_2 mixtures for the sterilization process, N(^{4}S), O(^{3}P), NO(X), NO(A) and NO(B) in the afterglow regions.

Figure 5 shows the temporal evolution of the fractional concentration of N(^{4}S) atoms in the afterglow of a N_2–O_2 microwave discharge, with $\omega/(2\pi) = 2450$ MHz, $R = 3 \times 10^{-3}$ m and $p = 667$ Pa and fractional percentages of added O_2 equal to 0.7%, 2% and 7%. It can be seen that the relative concentration of the nitrogen atoms remains practically unchanged during the afterglow until times of the order of 10^{-2} s for $[O_2]_0/N_g = 0.7\%$ and 2%, whereas in the time interval 10^{-2}–10^{-1} s there is a rapid decrease in the N(^{4}S) concentration in the case of 2% of added O_2. However, at the higher O_2 percentage of 7%, the decrease in $[N(^4S)]/N_g$ occurs earlier at $t \sim 1$ ms. As mentioned before, the kinetics of the nitrogen atoms strongly depends on the coupled populating and depopulating processes $N_2(X, v \geqslant 13)$+O$\rightarrow$N(^{4}S)+NO(X) and N(^{4}S)+NO(X) $\rightarrow N_2(X, v \sim 3)$+O, respectively. The faster decrease observed in the temporal evolution of N-atoms as the percentage of O_2 increases results from $N_2(X, v)$ depopulation as follows: (i) it occurs due to a global depletion of $N_2(X, v)$ levels by V–T processes associated with N_2–O_2 and N_2–O collisions [13] and (ii) due to a vibration–vibration (V–V) pumping-up mechanism, the tail of the VDF passes through a pronounced maximum at 10^{-3} s and starts to depopulate for longer afterglow times.

In order to clarify this behaviour, we present in figure 6 the calculated VDF at different times in the afterglow of a N_2–2%O_2 microwave discharge, from $t = 0$ s to $t = 10^{-1}$ s, for the same conditions as in figure 5.

Figure 7 shows the temporal evolution of the fractional concentration of the oxygen atoms, $[O(^3P)]/N_g$, for the same conditions as in figure 6. It is worth noting that this species is essentially produced through the process N(^{4}S) + NO(X) $\rightarrow$ $N_2(X, v \sim 3)$+O. Therefore, since the decrease in the nitrogen

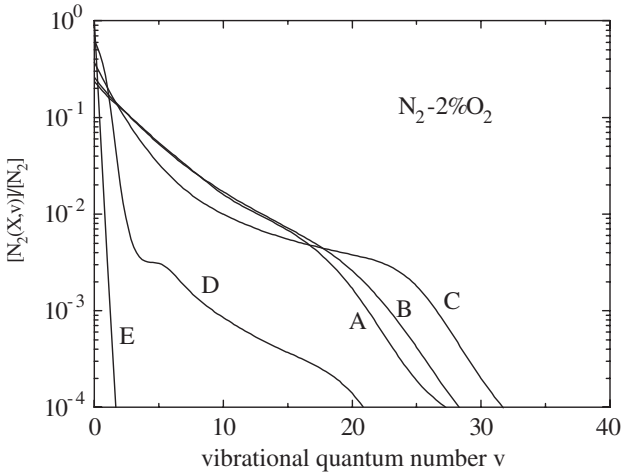

Figure 6. VDF of the $N_2(X, v)$ molecules at different times: (A) $t = 0$, (B)$t = 10^{-4}$ s, (C) $t = 10^{-3}$ s, (D) $t = 10^{-2}$ s and (E) $t = 10^{-1}$ s, in the afterglow of a N_2–2%O_2 microwave discharge with $p = 667$ Pa, $\omega/(2\pi) = 2450$ MHz and $R = 3 \times 10^{-3}$ m.

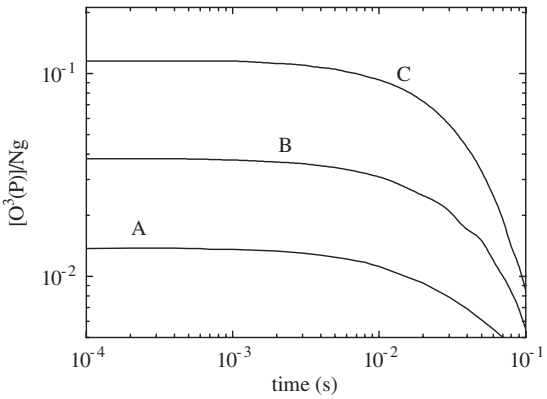

Figure 7. Temporal evolution of the fractional concentration of $O(^3P)$ atoms in the afterglow for the same conditions as in figure 5.

atom concentration is faster for higher percentages of added O_2, the concentration of the oxygen atoms along the afterglow decays more rapidly as $[O_2]/N_g$ increases from 0.7% up to 7%.

Let us now analyse the NO(B) kinetics during the afterglow. We recall that at the end of the discharge, we predicted that the concentration of this species was more abundant at the highest values of $[O_2]_0/N_g$ considered in this work (7%). Since NO(B) is exclusively produced by the three-body process N+O+(M)→NO(B)+(M), with M = (N_2, O_2), the relaxation of NO(B) during the afterglow should follow the temporal evolution of $N(^4S)$ and $O(^3P)$ atoms. As a matter of fact, this behaviour is illustrated in figure 8, where we represent the fractional concentration of NO(B) molecules in the same conditions as in the previous figures. This figure clearly shows that for afterglow times longer than 10 ms, the UV radiation from the NO(B) state is more important for $[O_2]_0/N_g = 0.7\%$ and 2%, while for the higher percentage of 7% there is a much faster decrease in this species. This effect is not only a consequence of a more rapid depopulation of $N(^4S)$ and $O(^3P)$ atoms but is also due to the enhancement of the NO(B) quenching by NO(X) as $[O_2]_0/N_g$ increases.

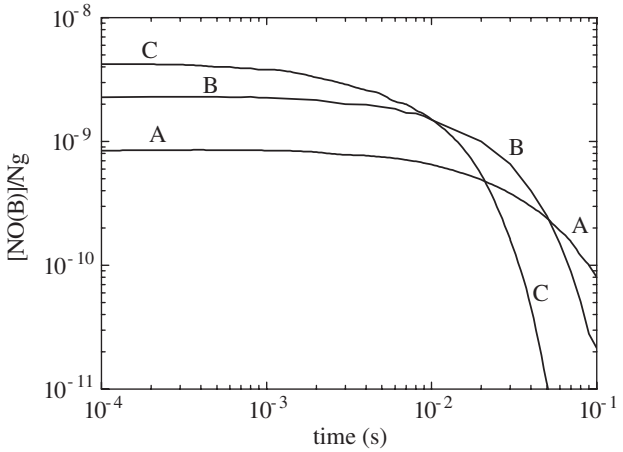

Figure 8. Temporal evolution of the fractional concentration of NO(B) emitting state in the afterglow for the same conditions as in figure 5.

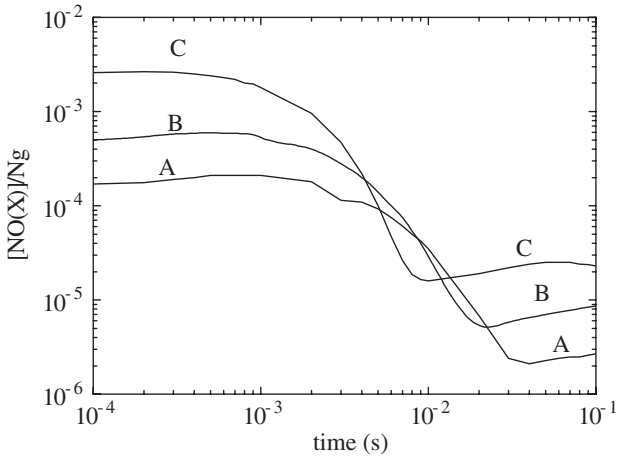

Figure 9. Temporal evolution of the fractional concentration of the NO(X) molecules in the afterglow for the same conditions as in figure 5.

For completeness, figure 9 shows the temporal variation of $[NO(X)]/N_g$ during the afterglow, where we can see a fast decay of the concentration of this species in the time interval 10^{-3}-10^{-2} s. It is worth recalling that this species is mainly produced by the reactions $N_2(X, v \geqslant 13)$+O→$N(^4S)$+NO(X) and $N_2(A)$+O→$N(^2D)$+NO(X). Moreover, within the mentioned interval there exists a very fast depletion of the tail of the VDF, shown in figure 6, and also a rapid depopulation of the $N_2(A)$ metastable. Therefore, figure 9 basically reflects the temporal deactivation of $N_2(X, v)$ and $N_2(A)$ species during the afterglow.

Finally, still concerning the results obtained in the afterglow zone, we present in figure 10 the time-evolution of the $[NO(A)]/N_g$ fractional concentration for the same conditions as considered before. Since NO(A) is only produced via the process $N_2(A)$+NO(X) →$N_2(X)$+NO(A), the kinetics of this species is strongly correlated with that of $N_2(A)$ (not represented here). In particular, at such afterglow times, the V–V pumping-up effect leads to $N_2(A)$ production via collisions of highly vibrational excited $N_2(X)$ molecules and $N(^4S)$ atoms [14].

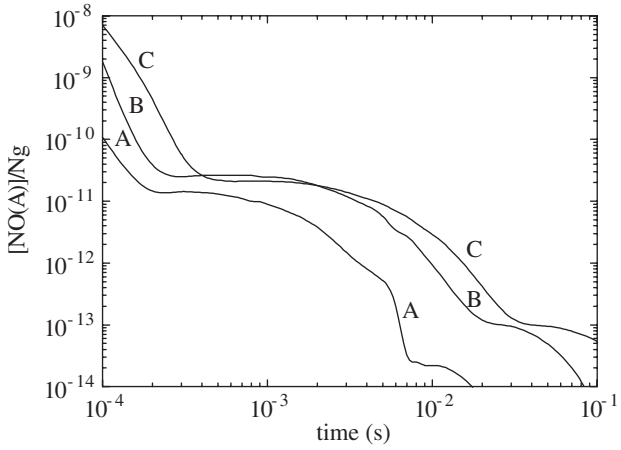

Figure 10. Temporal evolution of the fractional concentration of the NO(A) excited state in the afterglow for the same conditions as in figure 5.

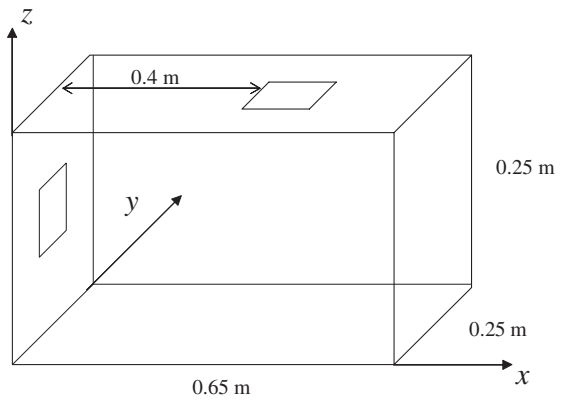

Figure 11. Schematic representation of the post-discharge chamber considered in the 3D model.

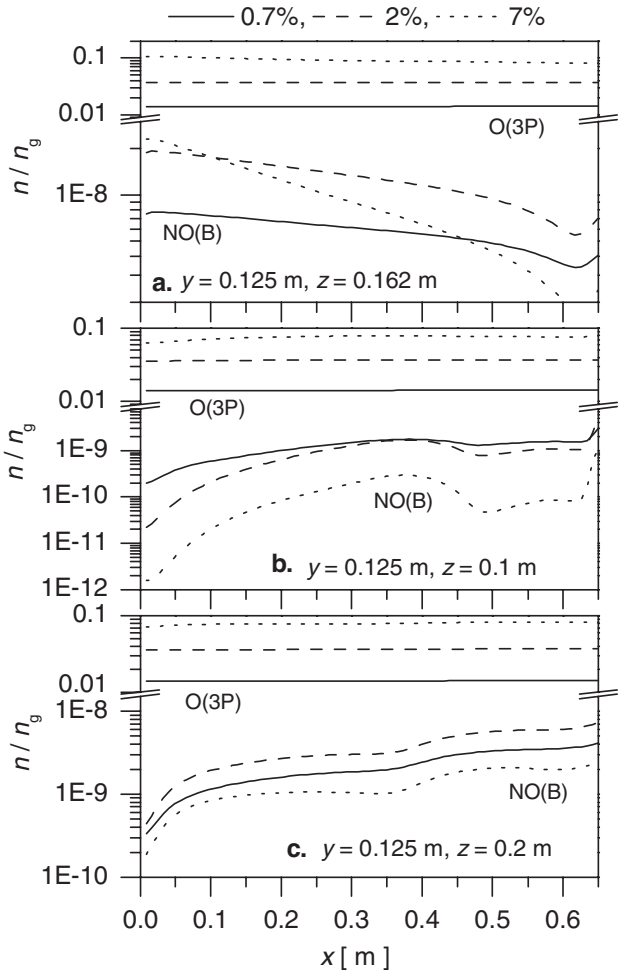

Figure 12. Fractional concentration of NO(B) and O(^{3}P) as a function of x at $y = 0.125$ m and at three different heights in the reactor: (a) $z = 0.162$ m, (b) $z = 0.10$ m and (c) $z = 0.2$ m, for different oxygen percentages.

Comparing figures 8 and 10, we can conclude that during the afterglow the NO(B) state is more populated than the NO(A) state, up to two orders of magnitude. Therefore, the role played by UV radiation in sterilization processes at reduced pressures should be attributed to the emission of NO_β bands. The results presented in figure 9 show that a higher NO(B) concentration can be obtained at lower oxygen percentages at afterglow times longer than 10 ms (which correspond to a distance of 0.5 m, assuming constant flow), suggesting that the same effect should also occur in the flow direction in the reactor. We will now detail this behaviour in the 3D analysis of the afterglow chamber, where we will describe the kinetics of NO(B) molecules and O(^{3}P) atoms. For clarity in the 3D results' discussion, we present in figure 11 a schematic description of the post-discharge chamber, with its dimensions and with the specification of the cartesian axes considered in our calculations.

Figure 12(a) presents the fractional concentration of NO(B) and O(^{3}P) at different oxygen percentages as a function of x at $y = 0.125$ m and $z = 0.162$ m. We note that these two y and z values correspond to the sterilization chamber entrance. This figure shows that the behaviour of these species is similar to the one presented in figure 8. With respect to NO(B), we observe a more pronounced decay of this species for oxygen percentages of 2% and 7%.

Figure 12(b) shows the predicted fractional concentration of NO(B) and O(^{3}P) densities at lower horizontal planes that are not crossed by the gas flow, for the case $z = 0.10$ m. We observe that the concentrations of O(^{3}P) atoms are more important as the initial oxygen added to the discharge increases. However, the NO(B) density shows a reverse behaviour. At this height the density of NO(B) molecules is more important for $[O_2]_0/N_g = 0.7\%$, and becomes lower as the O_2 percentage increases.

A quasi-similar behaviour can be observed in figure 12(c), where we present the fractional concentration of NO(B) and O(^{3}P) as a function of $[O_2]_0/N_g$ for $z = 0.2$ m, which is a plane situated between the inlet and the outlet. Our calculations still show that the lowest density of the NO(B) excited state occurs for $[O_2]_0/N_g = 7\%$; however in this plane the NO(B) density is higher in the case of 2% than that of 0.7% of $[O_2]_0/N_g$.

From figures 12(b) and (c), it can be seen that in the planes lower and higher than the inlet of the sterilization chamber (see figure in [3]), the UV emission from the NO_β band is in

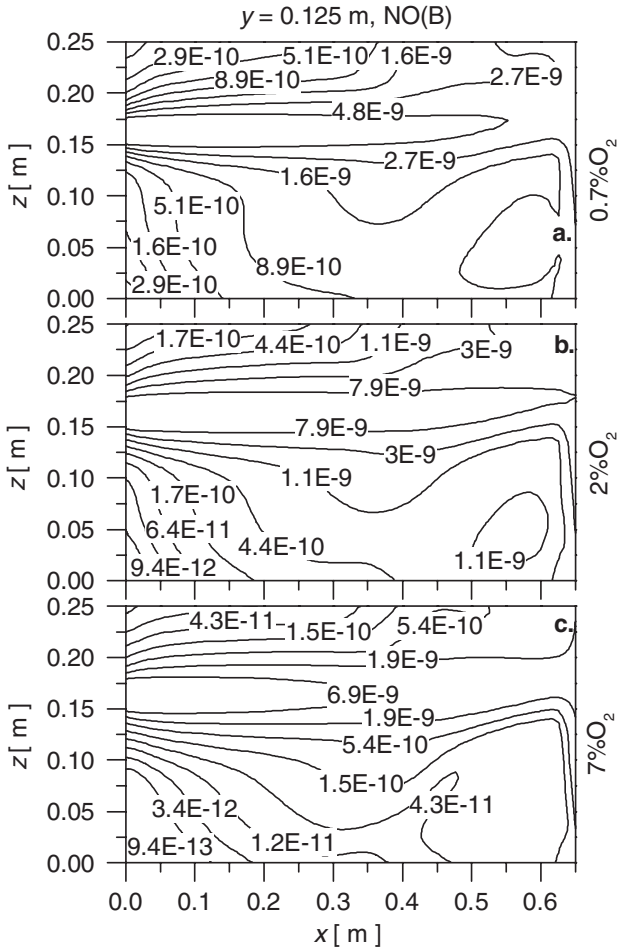

Figure 13. Distribution of the NO(B) fractional concentration in the reactor in the x–z plane at $y = 0.125$ m, at different O_2 percentages: (a) 0.7%, (b) 2% and (c) 7%.

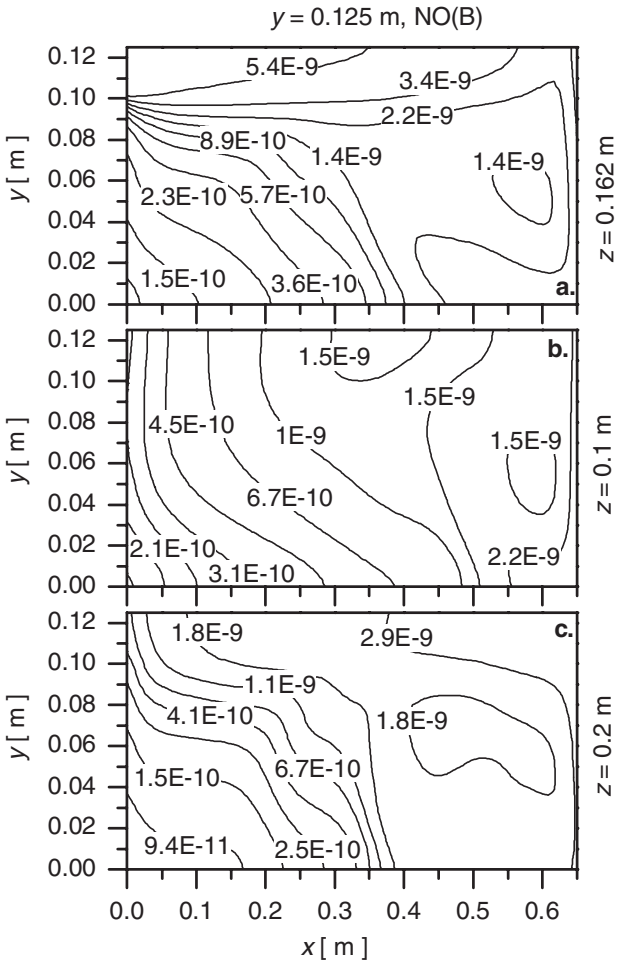

Figure 14. Distribution of the NO(B) fractional concentration at 0.7% O_2 in the x–y plane at different heights in the reactor: (a) $z = 0.162$ m, (b) $z = 0.10$ m and (c) $z = 0.20$ m.

general more important for $[O_2]_0/N_g \leqslant 2\%$. Since the sample holders are placed 0.10 m away from the afterglow chamber entrance [2] and at lower x–y planes [3,4], the results presented in these figures help us to understand the higher sterilization efficiency obtained for the lower concentrations of O_2 in the mixture, as shown in [2].

In order to describe in more detail the UV emission in the whole reactor, we represent in figures 13(a)–(c) the density distribution of NO(B) in the x–z plane at $y = 0.125$ m for $[O_2]_0/N_g = 0.7\%$, 2% and 7%, respectively. These figures show a decay of NO(B) from the entrance to the bottom and upper planes. Furthermore, we can observe that this effect is much more pronounced for $[O_2]_0/N_g = 7\%$, where the concentration of this species decreases by five and three orders of magnitude, respectively, in the bottom and top planes. This behaviour results from the major losses of NO(B) in the reactor due to quenching by O_2 and also due to NO(X), the density of which increases with the increasing O_2 percentage added into the discharge mixture.

The density of oxygen atoms (not shown in figure) is quasi-homogeneous in the whole reactor at every $[O_2]_0/N_g$ percentage, as suggested also by figures 12(a)–(c). The losses of this species in the reactor are compensated by their creation sources due to the reaction of N(^{4}S) with NO(X), NO_2 and O_2.

Finally, figures 14(a)–(c) show the density distribution of NO(B) in the x–y plane at different heights, respectively, $z = 0.162$ m, $z = 0.1$ m and $z = 0.20$ m, in the reactor for $[O_2]_0/N_g = 0.7\%$. For the case of $z = 0.162$ m, shown in figure 14(a), it can be seen that the NO(B) density decreases towards the reactor walls. In a lower plane, at $z = 0.10$ m, which does not include the inlet, the NO(B) concentration varies by about one order of magnitude; however, over a larger part of the plane, there is quasi-homogeneity. The same behaviour can also be observed in the planes situated between the inlet and the outlet, like the plane at $z = 0.20$ m shown in figure 14(c).

4. Summary and conclusions

We have presented a model for a low-pressure flowing microwave discharge and post-discharge in N_2–O_2 with the purpose of giving an insight into the understanding of elementary processes that are behind plasma sterilization in a post-discharge reactor. This study includes both the microwave discharge and the afterglow plasma up to the farthest remote zones of the post-discharge reactor, which covers the whole experimental device described in [1–4].

Essentially, we have developed a self-consistent steady-state kinetic model based on the master rate balance equations for the heavy species coupled to the homogeneous electron Boltzmann equation, in order to describe the active discharge zone. Then a time-dependent kinetic model was considered for the same master equations to calculate the evolution of the different species towards the post-discharge chamber. Once the concentrations of the species are known at the entrance of the chamber, we use a 3D hydrodynamic model to determine their density profiles along the reactor by considering the actual dimensions of the sterilization vessel.

Our study has focused mainly on the NO(A) and NO(B) emitting excited states, which are, respectively, associated with the UV emission of the NO_γ and NO_β bands and on the $O(^3P)$ atoms, owing to their importance in spore erosion during the sterilization process. The results found for these species in the afterglow region clearly show that the UV emission essentially comes from NO_β bands, in agreement with the spectroscopic observations [1–4]. It is important to stress this point here, since it was shown recently [5,15] that at atmospheric pressure, the UV radiation responsible for spore inactivation comes from the NO_γ band.

Furthermore, our results also show that the NO(B) concentration reaches a maximum intensity for a mixture composition in the discharge of approximately 0.7–2% of added O_2. This predicted result is in good agreement with the survival curves for spores' inactivation presented in [2], where it has been seen that the required exposure time for sterilization increases by a factor of two or three, respectively, when the percentage of added O_2 increases from 2% to 4% or to 7%.

Finally, we would like to mention two points that should be considered when describing future possible works. First, we will concentrate on a more detailed description of the connecting zone between the discharge tube and the post-discharge chamber. Second, it would also be desirable to check the importance of the $N_2(X, v)$ vibrational kinetics in the post-discharge chamber, which has been disregarded in the present paper. Here, the kinetics of vibrational molecules has been considered only in the discharge and in the early-afterglow region and not in the sterilization chamber.

Acknowledgments

The authors wish to thank Professor M Moisan for helpful discussions. This work was supported by the project POCTI/FAT/44221/2002 of the Portuguese Science Foundation FCT and a post-doctoral fellowship of KK.

References

[1] Moreau S, Moisan M, Tabrizian M, Barbeau J, Pelletier J, Ricard A and Yahia L' H 2000 *J. Appl. Phys.* **88** 1166
[2] Philip N, Saoudi B, Crevier M-C, Moisan M, Barbeau J and Pelletier J 2002 *IEEE Trans. Plasma Sci.* **30** 1429
[3] Moisan M, Barbeau J, Crevier M-C, Pelletier J, Philip N and Saoudi B 2002 *Pure Appl. Chem.* **74** 349
[4] Moisan M, Barbeau J, Moreau S, Pelletier J, Tabrizian M, Phillip N and Yahia L H 2001 *Int. J. Pharm.* **226** 1
[5] Boudam M K, Moisan M, Saoudi B, Popovici C, Gherardi N and Massines F 2006 *J. Phys. D: Appl. Phys.* **39** 3494
[6] Laroussi M 2005 *Plasma Process. Polym.* **2** 391
[7] Pintassilgo C D, Loureiro J and Guerra V 2005 *J. Phys. D: Appl. Phys.* **38** 417
[8] Kutasi K, Pintassilgo C D, Coelho P J and Loureiro J 2006 *J. Phys. D: Appl. Phys.* **39** 3978
[9] Guerra V and Loureiro J 1997 *Plasma Sources Sci. Technol.* **6** 373
[10] Kim Y C and Boudart M 1991 *Langmuir* **7** 2999
[11] Shivarova A and Zhelyakov I 1978 *Plasma Phys.* **20** 1049
[12] Guerra V, Dias F M, Loureiro J, Sá P A, Supiot P, Dupret C and Popov T 2003 *IEEE Trans. Plasma Sci.* **31** 542
[13] Guerra V and Loureiro J 1995 *J. Phys. D: Appl. Phys.* **28** 1903
[14] Sá P A, Guerra V, Loureiro J and Sadeghi N 2004 *J. Phys. D: Appl. Phys.* **37** 221
[15] Boudam K M B, Popovici C, Moisan M, Saoudi B, Gherardi N and Massines F 2006 *Proc. 18th Europhysics Conf. on Atomic and Molecular Physics of Ionised Gases (ESCAMPIG) (Lecce, Italy)* ed M Cacciatore *et al* p 67